Article

Structurally complex phase engineering enables hydrogen-tolerant Al alloys

https://doi.org/10.1038/s41586-025-08879-2

Received: 23 August 2024

Accepted: 10 March 2025

Published online: 30 April 2025

Open access

Check for updates

Shengyu Jiang[1,10], Yuantao Xu[2,10]✉, Ruihong Wang[3,10], Xinren Chen[4], Chaoshuai Guan[5], Yong Peng[5], Fuzhu Liu[1], Mingxu Wang[6], Xu Liu[7], Shaoyou Zhang[7], Genqi Tian[2], Shenbao Jin[7], Huiyuan Wang[7], Hiroyuki Toda[8], Xuejun Jin[2], Gang Liu[1]✉, Baptiste Gault[4,9]✉ & Jun Sun[1]✉

Hydrogen embrittlement (HE) impairs the durability of aluminium (Al) alloys and hinders their use in a hydrogen economy[1–3]. Intermetallic compound particles in Al alloys can trap hydrogen and mitigate HE[4], but these particles usually form in a low number density compared with conventional strengthening nanoprecipitates. Here we report a size-sieved complex precipitation in Sc-added Al–Mg alloys to achieve a high-density dispersion of both fine Al_3Sc nanoprecipitates and in situ formed core-shell $Al_3(Mg, Sc)_2/Al_3Sc$ nanophases with high hydrogen-trapping ability. The two-step heat treatment induces heterogeneous nucleation of the Samson-phase $Al_3(Mg, Sc)_2$ on the surface of Al_3Sc nanoprecipitates that are only above 10 nm in size. The size dependence is associated with Al_3Sc nanoprecipitate incoherency, which leads to local segregation of magnesium and triggers the formation of $Al_3(Mg, Sc)_2$. The tailored distribution of dual nanoprecipitates in our Al–Mg–Sc alloy provides about a 40% increase in strength and nearly five times improved HE resistance compared with the Sc-free alloy, reaching a record tensile uniform elongation in Al alloys charged with H up to 7 ppmw. We apply this strategy to other Al–Mg-based alloys, such as Al–Mg–Ti–Zr, Al–Mg–Cu–Sc and Al–Mg–Zn–Sc alloys. Our work showcases a possible route to increase hydrogen resistance in high-strength Al alloys and could be readily adapted to large-scale industrial production.

Recent results demonstrated that intermetallic compound particles (ICPs) in Al alloys can trap and store H (refs. 4,5). Nevertheless, the ICPs, theoretically with a high H-trapping ability[6], contain solutes (such as Mn, Cr, Fe) that have a low solubility in Al (ref. 7) and thus precipitate and coarsen already during solidification of the alloy. These ICPs are coarse, in low number density (less than about 10^{17} m^{-3}; Supplementary Fig. 1) and volume fraction (less than about 0.4 vol%), limiting their ability to enhance the HE resistance. Moreover, the ICPs traditionally precipitating on the nanoscale in heat-treatable Al alloys exhibit limited H-trapping capability. Despite their high number density (more than approximately 10^{20} m^{-3}) and volume fraction (up to about 1.0 vol%)[8], these precipitates are unable to enhance the HE resistance. High H-trapping capability and high number density (volume fraction) are hence two pre-requisites for improving the HE resistance of precipitation-strengthened Al alloys, yet they seem to be mutually exclusive based on the known ICPs (Supplementary Fig. 1).

Amongst ICPs, complex metallic phases (CMPs) are characterized by the presence of icosahedral coordination, large lattice constants and correspondingly several atoms per unit cell, typically ranging from tens to thousands (refs. 9,10). The Al_3Mg_2 phase, with a β-Samson structure, is one of the most complex intermetallic structures[11]. Its cubic elementary cell contains 1,168 atoms that are distributed over 1,832 atomic positions, with partially occupied sites generating split positions that induce structural disorder[12]. The extremely complex crystal structure can be described as an array of giant atomic clusters consisting of coordination shells[13] (Supplementary Fig. 2). The Samson-Al_3Mg_2 phase can be expected to have a high solubility for H and act as an efficient trap[14]. In the Al–Mg alloys with Mg content greater than about 5.5 wt%, the Samson-Al_3Mg_2 phase precipitates on heat treatments, yet usually uncontrollably, preferentially nucleating at GBs, in which they fast coarsen[15]. This suggests that nucleation is energetically difficult and mainly takes place heterogeneously[16].

Here we show that a high-density intragranular precipitation of nano-sized Samson-Al_3Mg_2 precipitates can be achieved in a Sc-microalloyed Al–Mg alloy. High-density Al_3Sc precipitates are first precipitated, which interrupts the Mg diffusion to GBs and induces a strong Mg segregation at the Al_3Sc–matrix interface. This favours the heterogenous nucleation of a shell partially Sc-substituted Al_3Mg_2, that is, $Al_3(Mg, Sc)_2$, nanophase with a Samson-Al_3Mg_2 structure, on large Al_3Sc precipitates (size above approximately 10 nm). The high-density $Al_3(Mg, Sc)_2$ nanophase from the core-shell nanoprecipitates, with abundant nanoclusters and vast atomic disorders, has a high solubility for H and thus

[1]State Key Laboratory for Mechanical Behavior of Materials, Xi'an Jiaotong University, Xi'an, China. [2]Shanghai Key Laboratory of Materials Laser Processing and Modification, Shanghai Jiao Tong University, Shanghai, China. [3]School of Materials Science and Engineering, Xi'an University of Technology, Xi'an, China. [4]Max-Planck Institute for Sustainable Materials, Düsseldorf, Germany. [5]School of Materials and Energy, Electron Microscopy Centre of Lanzhou University, Lanzhou University, Lanzhou, China. [6]School of Mechanical, Electrical and Information Engineering, Shandong University, Weihai, China. [7]State Key Laboratory of High Performance Roll Materials and Composite Forming, School of Materials Science and Engineering, Hebei University of Technology, Tianjin, China. [8]Department of Mechanical Engineering, Kyushu University, Fukuoka, Japan. [9]Department of Materials, Imperial College, South Kensington, London, UK. [10]These authors contributed equally: Shengyu Jiang, Yuantao Xu, Ruihong Wang. ✉e-mail: xuyuantao@sjtu.edu.cn; lgsammer@xjtu.edu.cn; b.gault@mpie.de; junsun@xjtu.edu.cn

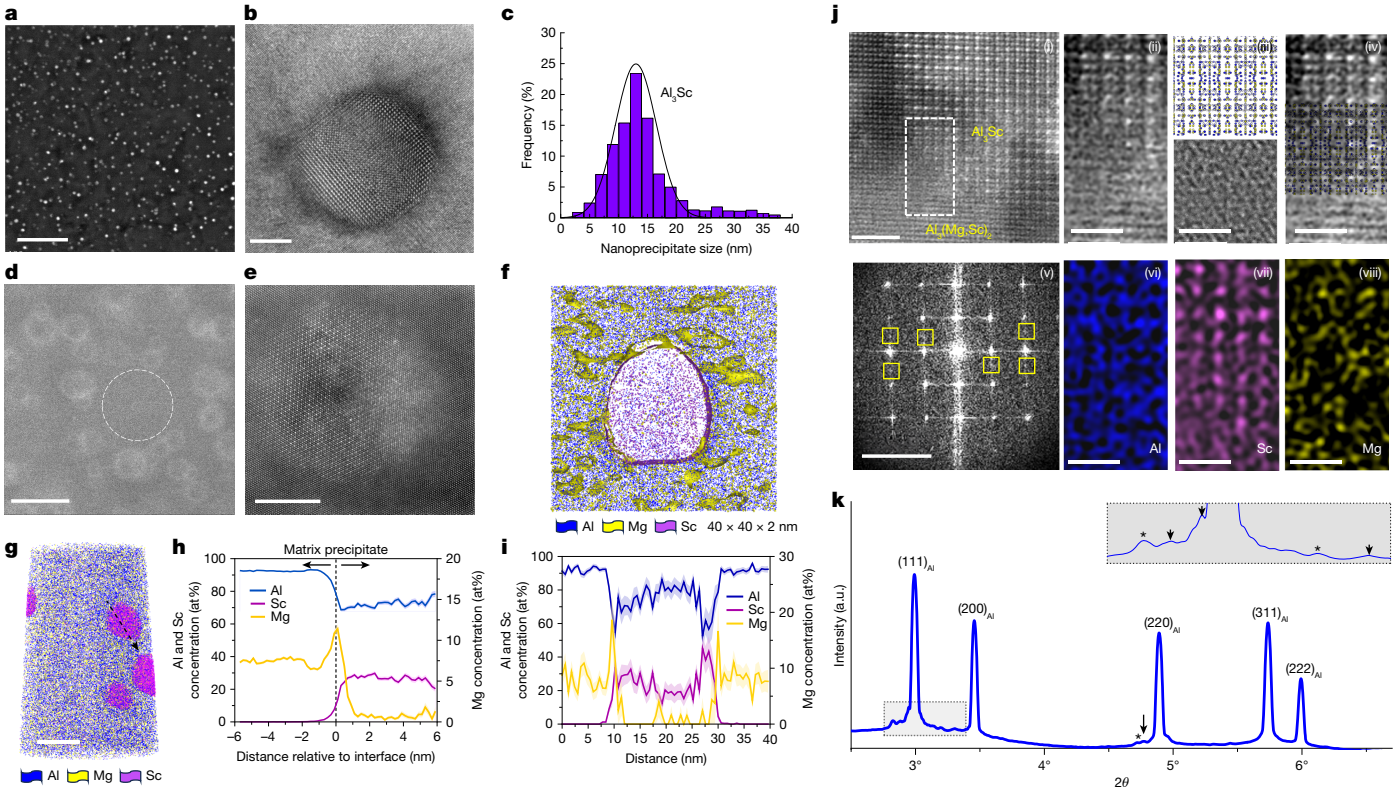

Fig. 1 | High-density $Al_3(Mg, Sc)_2$ nanophase by in situ phase transformation. **a**,**b**, Representative low-magnification (**a**) and high-magnification (**b**) TEM images to show the high-density formation of Al_3Sc nanoprecipitates in Al–Mg–Sc-I alloy. **c**, The statistical size distribution of the Al_3Sc nanoprecipitates. **d**,**e**, Representative HAADF-STEM images of nanoprecipitates in Al–Mg–Sc-II alloy to show a 'different' phase formed on the Al_3Sc nanoparticles by contrast. **f**, Thin-slice APT image to show the Mg concentration undulation within the matrix close to Al_3Sc nanoparticle. **g**–**i**, Representative APT image (**g**) and composition analysis (**h**,**i**) in the Al–Mg–Sc-II alloy. Composition proximity histograms across the interface (**h**) and 1D profile element concentration distributions (**i**) across the nanoprecipitate indicated by the arrow in **g**, which shows a high Mg concentration at the outer different phase. Standard error is shown in **i**. **j**, Crystal structure analysis of the Mg-rich phase (zone axis $[121]_\beta$). A representative HAADF-STEM image (i) and locally magnified image ((ii), corresponding to the box region marked in (i)) on the interface dividing the Mg-rich phase (bottom left) and Al_3Sc phase (top right). By comparing with the crystal structure (crystal structure sketch and simulated image in (iii) and overlapped figure in (iv)), the Mg-rich phase is determined to be Samson-Al_3Mg_2 structure. (v), Corresponding FFT image indicates a coexistence of the two phases. (vi)–(viii), corresponding elemental atomic mapping highlights the presence of Sc atoms in the Mg-rich phase, corresponding to the $Al_3(Mg, Sc)_2$ phase with some Mg positions partially occupied by Sc. **k**, Synchrotron X-ray diffraction results index both the β-Al_3Mg_2 (peaks indicated by asterisks) and the β′-Al_3Mg_2 (peaks indicated by arrows) structure in the Al–Mg–Sc-II alloy. The inset shows a magnified image corresponding to the shadow region. The indexed peaks are also shown in Supplementary Table 2. Scale bars, 200 nm (**a**); 5 nm (**b**,**e**); 50 nm (**d**); 25 nm (**g**); 2 nm (**j**(i)); 5 1/nm (**j**(v)); 1 nm (**j**(ii)–(iv), (vi)–(viii)).

provides this alloy with an exceptional HE resistance. Although the other fine Al_3Sc nanoprecipitates (size below about 10 nm), free of in situ phase transformation, make a predominant contribution to the strength that is notably increased by nearly 40% in comparison with the Sc-free Al–Mg alloy. These dual nanoprecipitates allow for breaking the trade-off between strength and HE resistance generally observed in Al alloys.

High-density CMP nanoprecipitates

A twin-roll cast Al–6.0 Mg (wt%) alloy (hereafter denoted as Al–Mg) and Al–6.0 Mg–0.3 Sc (wt%) alloy (hereafter denoted as Al–Mg–Sc) were prepared for comparison (Methods). The two alloys were first annealed at 400 °C for 4 h (denoted as Al–Mg-I and Al–Mg–Sc-I, respectively), in which the Mg atoms are fully dissolved but the supersaturated Sc atoms have precipitated as Al_3Sc nanoprecipitates. The two alloys were further subjected to a second heat treatment at 250 °C for 72 h (denoted as Al–Mg-II and Al–Mg–Sc-II, respectively). For comparison, an Al–0.3 Sc (wt%) alloy was also prepared and followed the same heat treatments as Al–Mg–Sc-II, which is referred to as Al–Sc-II.

A dispersion of Al_3Sc nanoprecipitates was created in Al–Mg–Sc-I alloy (Fig. 1a,b), with a high number density of about 8.0×10^{21} m^{-3} and an average size of around 14 nm (approximately 70% of the nanoprecipitates larger than about 10 nm; Fig. 1c). Atom probe tomography (APT) indicates a strong Mg segregation, of up to 15 at%, at the Al_3Sc–matrix interface (Supplementary Fig. 3a,b). In Al–Mg–I alloy, recrystallization led to grains up to an average size of about 200 μm, separated mostly by high-angle GBs (greater than 15°) as demonstrated by electron backscatter diffraction in Supplementary Fig. 3c,d. By contrast, the Al–Mg–Sc-I alloy exhibits an average grain size of about 100 μm and a higher fraction of low-angle GBs (less than 15°). The fine-grained microstructure is maintained because of the Al_3Sc nanoprecipitates effectively pinning the GBs by Zener drag force[17].

In Al–Mg-II, similar to previous studies[18,19], the high-concentration Mg segregation at the GBs leads to coarse Samson-Al_3Mg_2 particles precipitated at the GBs, and some within the grain interior. The quasi-continuous network of GB precipitates facilitates premature fracture due to local strain discrepancy[20] and corrosion failure due to anodic dissolution mechanism[21]. Within the intragranular particle (Supplementary Fig. 4), a highly inhomogeneous distribution of Mg is detected, and β′-Al_3Mg_2 phase (in a rhombohedral structure) coexists with β-Al_3Mg_2 phase (in a cubic structure) because of the sluggish atomic diffusion in the CMPs. As the two phases are structurally close (Supplementary Fig. 2) and difficult to fully

separate, both are hereafter referred to as the Samson-Al_3Mg_2 phase for simplicity.

In the Al–Mg–Sc-II alloy, the minor Sc addition led to a completely different precipitation behaviour. The β-Al_3Mg_2 intergranular precipitation was greatly reduced. According to previous results[22], Mg atoms tend to segregate to the Al_3Sc–matrix interfaces, especially at {110} and {111} facets, to lower the interfacial free energy. Therefore, the fine dispersion of Al_3Sc nanoprecipitates readily formed inside the grains will hinder the long-range Mg diffusion to GBs. The region highlighted by a dashed white circle in the HAADF-STEM image in Fig. 1d shows how most of the Mg-rich regions of the matrix are enclosed by the Al_3Sc nanoprecipitates. A 2-nm-thick slice through an APT reconstruction (Fig. 1f) shows Mg concentration fluctuations in the matrix close to an Al_3Sc nanoprecipitate.

Contrast in the HAADF-STEM images, Fig. 1d and e, suggests that the Al_3Sc nanoprecipitates are covered by a shell of a different composition and structure. APT, as shown in Fig. 1g–i, enables quantitative compositional analysis that shows Mg interfacial enrichment. Aberration-corrected HAADF-STEM was performed to study the structure of the Mg-rich shell, see Fig. 1j. Figure 1j(i) shows a representative micrograph of the core (top right) and shell (bottom left) of an Al_3Sc precipitate, separated by a heterophase interface. A locally magnified HADDF-STEM image is presented in Fig. 1j(ii), and the corresponding simulated image in Fig. 1j(iii) and overlapped image in Fig. 1j(iv), which allows to readily compare the structure of the Mg-rich phase and the Al_3Sc. The crystal structure of the Mg-rich phase is consistent with the sketch of the Samson-Al_3Mg_2 phase, viewed along the same direction (Fig. 1j(iii)). Synchrotron X-ray diffraction results (Fig. 1k) and more HAADF-STEM images (Supplementary Fig. 5) further confirm that the Mg-rich phase is the Samson-Al_3Mg_2 phase.

Elemental mapping by X-ray energy-dispersive spectroscopy in STEM (STEM-EDS) from the same area is shown in Fig. 1j(vi–viii) for each element separately. In the Al_3Sc phase, Sc is in a periodic and well-defined arrangement (Fig. 1j(vii)) and is also detected partially integrated in the shell, which agrees with the APT results in Fig. 1h, implying Sc atoms partially occupying the Mg positions in the Samson-Al_3Mg_2 phase. This partial site occupation leads to a reduction in the free energy of the system, according to density functional theory (DFT) calculations (Methods and Supplementary Fig. 6a), making them favourable. These calculations help rationalize the formation of the Samson phase despite the low Mg concentration (about less than 15 at%) at the Al_3Sc–matrix interface, as the combination of Sc and Mg reaches above 30 at% (Fig. 1h,i). Through this complex precipitation path, the Al–Mg–Sc-II alloy exhibits a high dispersion of nanoscale precipitates on which a shell has formed, exhibiting the structure of the Samson-Al_3Mg_2, thermodynamically stabilized by Sc, and denoted as $Al_3(Mg, Sc)_2$.

Mechanism of the in situ phase transformation

It was recently reported in an Al–Cu–Mg–Ag–Sc alloy that the growth ledges, a type of crystal defects at the interfaces between plate-shaped Ω nanoprecipitates and the Al matrix[23,24], enable Sc atoms uptake into the Ω phase and stimulate an in situ phase transformation[25]. Similarly, in the present Al–Mg–Sc alloy, when exposed to the second-step heat treatment, the Mg atoms segregated at the Al_3Sc–matrix interfaces can diffuse into the Al_3Sc nanoprecipitates. The $L1_2$-structured β″-Al_3Mg phase has lattice constants close to the $L1_2$-structured Al_3Sc phase[26], and the partial occupation of Sc-sites by Mg is energetically favourable, based on DFT calculations (Supplementary Fig. 6b). Locally, Al_3Sc hence becomes $Al_3(Sc, Mg)$ and as Mg becomes more highly concentrated locally, we can expect a metastability cascade from $Al_3(Sc, Mg)$ → $L1_2$-structured β″-$Al_3(Mg, Sc)$ → β′-$Al_3(Mg, Sc)_2$ → β-$Al_3(Mg, Sc)_2$, which is a sequence close to previous reports[27]. This is analogous to

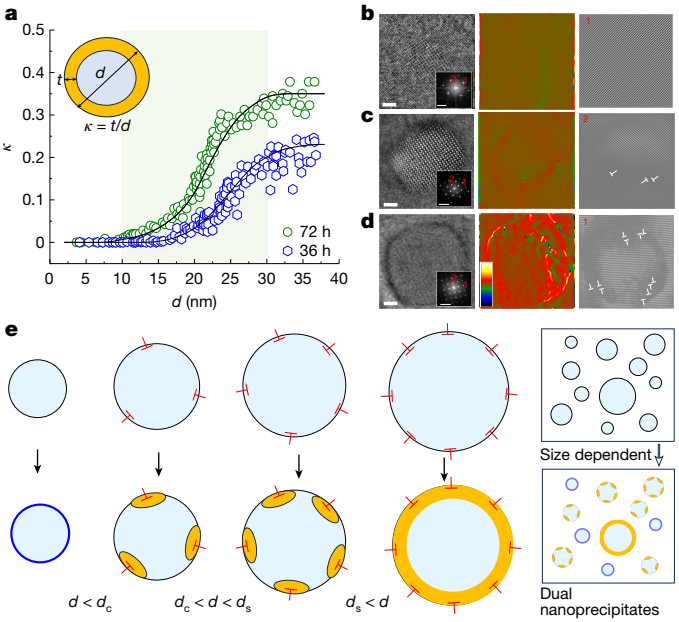

Fig. 2 | Interface-dominated in situ phase transformation. a, Statistical results on the ratio of outer $Al_3(Mg, Sc)_2$ nanophase (κ, defined as the average thickness, t, of $Al_3(Mg, Sc)_2$ phase divided by the total diameter d of the nanoprecipitate) as a function of d, at two ageing times (72 h and 36 h) during the II treatment. **b**–**d**, Representative high-magnification TEM (HRTEM) images (left), ε_{xx} strain mapping calculated from geometrical phase analysis (GPA) (middle) and inverse Fourier transform (IFT) images (right) of d = 6 nm (**b**), 10 nm (**c**) and 30 nm (**d**) nanoprecipitates, respectively, in the Al–Mg–Sc-I alloy. Size-sensitive interfacial dislocations are indicated in the IFT images. Insets in the HRTEM images are corresponding fast Fourier transform (FFT) images, in which spot 1 corresponds to the $[001]_{Al}$, and spot 2 to the $[010]_{Al}$. The IFT images are created based on either spot 1 or spot 2. The scale bar in the GPA images represents the maximum of +1.0 and the minimum of −1.0. **e**, Sketches to show the size-selective in situ phase transformation of the $Al_3(Mg, Sc)_2$ nanophase triggered by interfacial dislocations. Dual nanoprecipitates are designed for the present Al–Mg–Sc-II alloy. Scale bars, 2 nm (**b**,**c**); 5 nm (**d**).

the formation of core-shell $Al_3(Sc, Zr)$ nanoprecipitates in Al alloys with Sc and Zr additions, for which the underlying mechanism was suggested to be diffusion-dominated[28,29]. It is reasonable to apply this mechanism to rationalize the formation of metastable $Al_3(Sc, Mg)$ phase in this work, which finally evolves into the more stable Samson-structure $Al_3(Mg, Sc)_2$ phase.

The $Al_3(Mg, Sc)_2$ phase formation is inversely dependent on the nanoprecipitate size (Fig. 2a). Ultrafine Al_3Sc remains coherent with the Al-matrix. Beyond a critical size d_c evaluated experimentally to be about 10 nm (Fig. 2b–d), which agrees with theoretical predictions[30] (Supplementary Fig. 7), the interfacial coherency is lost and interfacial dislocations accommodate the lattice mismatch between phases. Figure 2a plots the relative length of the $Al_3(Mg, Sc)_2$ shell over the diameter of the precipitate, denoted as κ and schematically shown as an inset in the figure, as a function of the precipitate diameter. The nanoprecipitates with a size smaller than d_c are free of the $Al_3(Mg, Sc)_2$ phase (Supplementary Fig. 8a). The larger the precipitate, the more interfacial dislocations and the thicker is the $Al_3(Mg, Sc)_2$ phase, up to about 30 nm (d_s) (Fig. 2a and Supplementary Fig. 8b,c), in which κ gradually reaches a plateau. These observations suggest that the interfacial dislocations play a key part in the nucleation of the $Al_3(Mg, Sc)_2$ phase, by promoting Mg segregation at the Al_3Sc–matrix interface[31], changing the local composition to modify the interfacial chemical equilibrium[32]. They can also provide sites for heterogenous nucleation (Supplementary Fig. 9 and Supplementary Note 1) along with faster diffusion channels[33] for

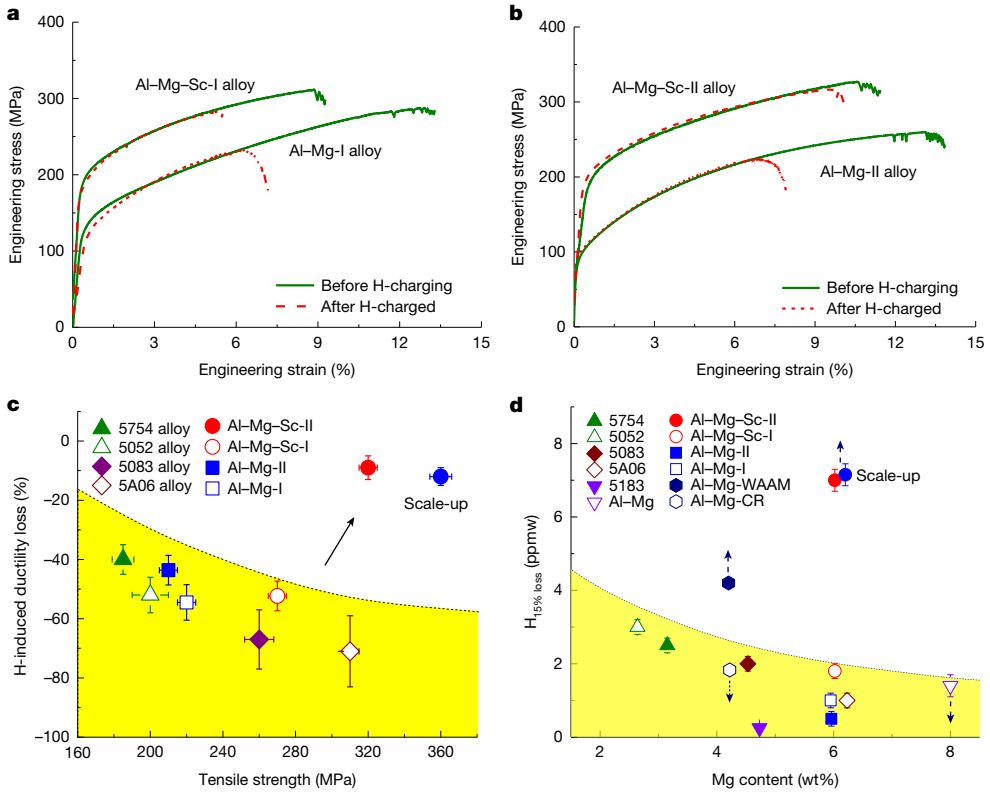

Fig. 3 | Extraordinary HE resistance boosted by the Samson-structured nanophase. a,**b**, Representative tensile stress–strain curves of the I-treated (**a**) and II-treated (**b**) Al–Mg and Al–Mg–Sc alloys before H-charging (solid lines) and after H-charging (dashed lines) for comparison. **c**,**d**, Exceptional HE resistance of present Al–Mg–Sc-II alloy. **c**, H-induced ductility loss: Al–Mg–Sc-II alloy of this study (solid red dot) compared with the other three alloys studied and four commercial 5xxx Al alloys with similar H-charging of about 7 ppmw. **d**, Mg content dependence of $H_{15\%\,loss}$: Al–Mg–Sc–II alloy compared with the other alloys studied, four commercial 5xxx alloys and available data of reported 5183 wire[34], Al–Mg alloys[36] and wire arc additive manufactured (WAAM) Al–Mg alloy (compared with the Al–Mg counterpart prepared by traditional casting and rolling (CR))[46]. Our Al–Mg–Sc-II alloy shows the greatest H-tolerance even at a high Mg content, standing out, above and beyond the known trend (yellow-shaded region) for the normal HE resistance reducing with increasing Mg content. The solid blue dot represents the scale-up material of the Al–Mg–Sc-II alloy, which has an HE resistance very close to the latter but a higher strength by 15% increase. The dashed arrows in **d** indicate $H_{15\%\,loss}$ will further increase or decrease, with no experimental determination exactly. The error bars are the standard deviation of the mean ($n = 5$).

redistribution of the Mg atoms near the Al_3Sc. Figure 2e schematically shows the in situ formation of nanosized $Al_3(Mg, Sc)_2$ and its dependence on precipitate size.

Improved H-tolerance and strength

Figure 3a presents tensile stress–strain curves of the Al–Mg-I and Al–Mg–Sc-I alloys before and after being charged by about 7.0 ppmw H (Methods), respectively. Before H-charging, the Al–Mg–Sc-I alloy shows a yield strength increased by around 80% (or by about 100 MPa), whereas the total tensile elongation reduced by about 20%, when compared with its Sc-free counterpart (Fig. 3a). After H-charging, both alloys suffer a severe HE-induced decrease in elongation by about 54.5 ± 5.3% in the Al–Mg-I and about 45.3 ± 6.2% in the Al–Mg–Sc-I alloy (Fig. 3a).

Under the same H-charging conditions, the reduction in tensile elongation for Al–Mg-II is estimated to be about 43.6 ± 5.5% (Fig. 3b). In the Al–Mg–Sc-II alloy, however, the HE is nearly suppressed, with a reduction of only about 9.0 ± 0.5% in tensile elongation. This demonstrates a break-off from the expected trend that increasing the strength must come at the expense of HE resistance[5,6]. Here we designed an alloy with high dispersion of dual nanoprecipitates, the fine ones mainly contributing to strength (Supplementary Fig. 10), whereas the large core-shell ones suppressing HE. Conventional Al alloys are generally sensitive to HE and a few ppmw H deteriorates the tensile elongation of Al alloys[34,35]. The H concentration of about 7 ppmw is among the most extreme loading conditions, under which conventional Al alloys cannot maintain their ductility. But the present Al–Mg–Sc-II alloy shows only a slight reduction in ductility.

The superior HE resistance achieved in Al–Mg–Sc-II alloy is shown in Fig. 3c, in comparison with the other alloys studied and four commercial 5xxx series Al alloys (that is, 5052, 5083, 5754 and 5A06). These commercial alloys typically show more than 40% loss in ductility (Supplementary Fig. 11a,b), comparable to the alloys studied except for the Al–Mg–Sc-II alloy. The Al–Mg–Sc-II alloy stands out from the known trend (yellow-shaded region) that ductility greatly decreases with increasing strength. In particular, the present Al–Mg–Sc-II alloy after 7 ppmw H-charging exhibits uniform tensile elongation greater than 10%, which is much greater than all the other Al-Mg-based alloys tested with similar or lower H-charging levels[34,36]. To further demonstrate the high H-tolerance, we simply define a reference parameter, $H_{15\%\,loss}$, which represents the minimum H concentration charged to induce 15% loss in the tensile elongation. The Al–Mg–Sc-II alloy, even having a high Mg content, possesses $H_{15\%\,loss}$ far surpassing other Al–Mg-based alloys prepared by conventional methods (Fig. 3d).

The enhanced HE resistance in Al–Mg–Sc-II alloy can be further confirmed by analysing the fracture mode (quasi-cleavage fracture) of tensile samples (Supplementary Fig. 11c–e) and the H-induced loss in static toughness (Supplementary Fig. 11f). Moreover, the corrosion resistance was also improved in the Al–Mg–Sc-II compared with its

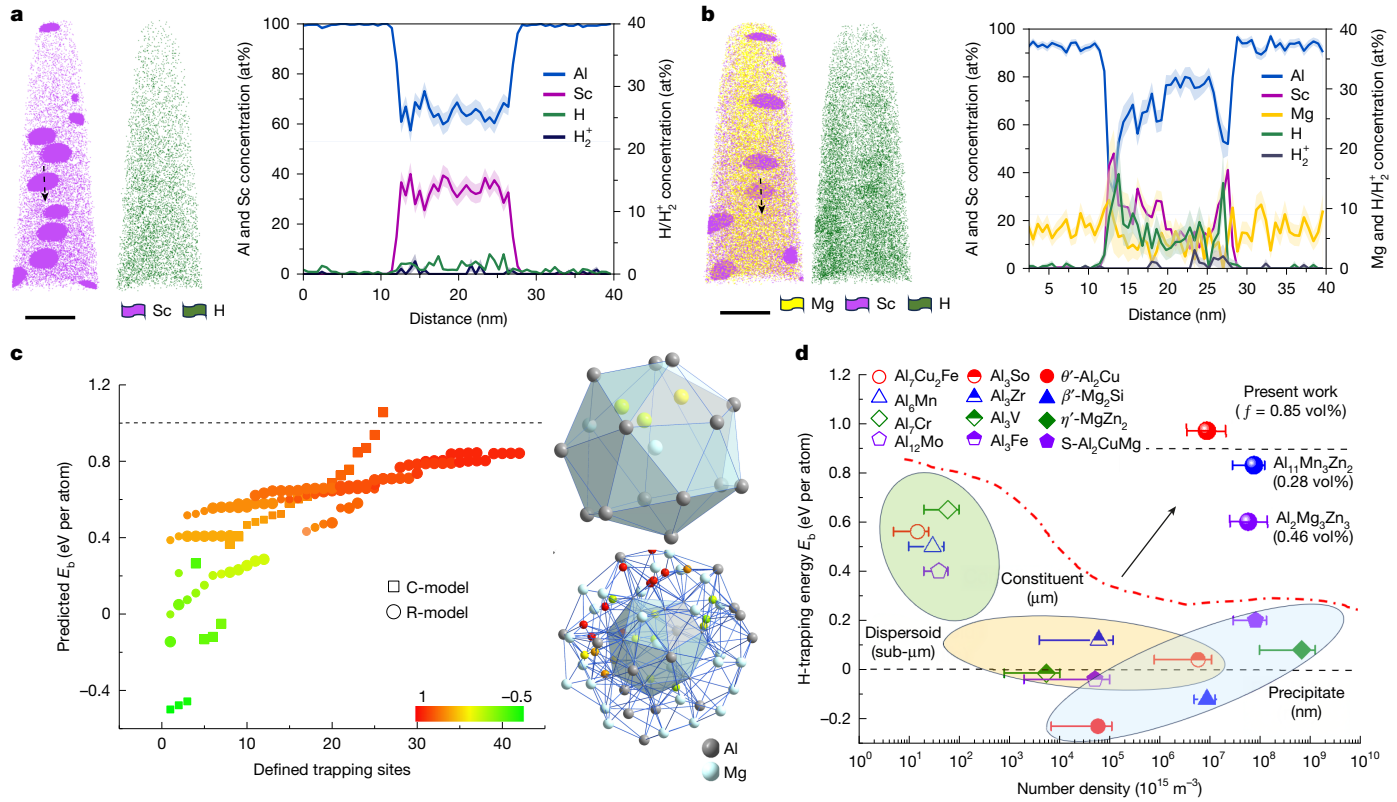

Fig. 4 | Unprecedented H-trapping ability of the complex metallic nanophase. **a**,**b**, Representative APT images and corresponding 1D profile element concentration distributions across an Al_3Sc nanoprecipitate (marked by arrow) in electropolished Al–Sc-II alloy (**a**) and across a coupled $Al_3(Mg, Sc)_2/Al_3Sc$ nanoprecipitate (marked by arrow) in electropolished Al–Mg–Sc-II alloy (**b**). A high H concentration >10 at% (about five times greater than in the Al–Sc–II alloy) is seen at the nanoprecipitate in **b**, indicative of a significant H-trapping capability. **c**, Simulation results of the H-trapping energy (E_b) at different occupying sites (sequence in number) by using two models (C-model and R-model), respectively. The colour represents the value of E_b for each predicted dot. Some H-occupying sites are typically shown in an A1-type nanocluster (right) in the R-model, with colour corresponding to the predicted E_b. The top shows the inner shell of the A1-type nanocluster, and the bottom shows the two-shell structure of the A1-type nanocluster. **d**, H-trapping energy compared with number density: present core-shell $Al_3(Mg, Sc)_2/Al_3Sc$ nanoprecipitates compared with other ICPs as summarized in ref. 6. The present nanoprecipitates surpass all the ICPs known in Al alloys, owing to their unprecedent H-trapping energy, high number density (several orders of magnitude greater than the μm-sized constituent particles and sub-μm-sized dispersoid particles), and high volume fraction (the same level as the traditional nanoprecipitates in commercial high-strength Al alloys). Note that the positive H-trapping energy represents a strong trapping capability, and vice versa. Number density of the other ICPs in **d** is taken or evaluated from references as given in Supplementary Fig. 1. The error bars of the present data are the standard deviation of the mean ($n = 5$), whereas the error bars of data from previous studies represent the maximum and minimum values, respectively. Scale bars, 50 nm (**a**,**b**).

Sc-free counterpart (Supplementary Fig. 12), mainly because of the suppression of intergranular Mg precipitation and segregation.

High H-trapping in the Samson phase

APT was used to demonstrate H-trapping in the $Al_3(Mg, Sc)_2$ nanophase. In Fig. 4a of the Al–Sc-II alloy, one-dimensional (1D) composition profile shows a low H concentration of only about 2.0 at% in the Al_3Sc nanoprecipitates that can be ascribed to a combination of H-ingress from the preparation and residual H from the APT chamber. By contrast, in Fig. 4b, the APT reconstruction and the 1D profile composition across a core-shell nanoprecipitate in the Al–Mg–Sc-II shows an H concentration >5.0 at% in the precipitate core, with a strong increase of up to 18 at% in the $Al_3(Mg, Sc)_2$ shell. More APT results from different hydrogen charging methods, cryogenic transfer conditions and APT operating modes (laser pulsing mode and high-voltage pulsing mode)[37–39] are shown in Supplementary Figs. 13 and 14, which support the conclusion that the $Al_3(Mg, Sc)_2$ shell strongly traps H (Supplementary Fig. 15).

APT-based statistical analyses (Supplementary Fig. 16) indicate that the smaller the nanoprecipitates are, the lower the trapped H concentration is. This finding agrees well with the aforementioned size-dependent phase transformation in which the $Al_3(Mg, Sc)_2$ phase forms more readily and in higher volume on larger Al_3Sc nanoprecipitates. Recent studies reported on a size dependence of nanoprecipitates trapping H in Al alloys[40,41] and steels[42], particularly related to the nature of the interfaces. The finer, coherent nanoprecipitates trap H through elastic interactions[40]. Large nanoprecipitates, with incoherent interfaces, trap H at misfit dislocations[41]. Here we use the interfacial misfit to trigger the precipitation of $Al_3(Mg, Sc)_2$ phase that has a high H-trapping capacity throughout its volume, meaning that H is no longer only trapped at the interface.

The H-trapping energy of $Al_3(Mg, Sc)_2$ phase was then estimated based on DFT (Methods). A computational description of the Samson phase is, however, extremely challenging, because of its extremely complex crystal structure. A model has been proposed that can completely describe the crystal structure of the Samson-Al_3Mg_2 phase[13], topologically treated as an assembly of two types of two-shell primary nanoclusters (Supplementary Fig. 2). This allows for modelling both the cubic (C-model) β-Al_3Mg_2 phase and the rhombohedral model (R-model) β′-Al_3Mg_2 phase (Supplementary Fig. 17a,b). DFT indicates an excellent H-trapping capacity in the interior of the Samson-Al_3Mg_2 precipitates with a maximum binding energy of around 1.12 eV in the cubic β-Al_3Mg_2 phase, and of about 0.85 eV in the rhombohedral β′-Al_3Mg_2 phase (Fig. 4c), on an average of slightly greater than about 0.90 eV per atom. In the latter, 60% of the H-trapping sites (108 sites

calculated) have a binding energy greater than 0.6 eV. The H-trapping capacity of Samson-Al_3Mg_2 phase surpasses that of all known intermetallic compounds and crystal defects that have been experimentally reported or theoretically predicted in Al alloys[6], as shown in Fig. 4d. Additional calculations showed that the partial occupation of Mg sites by Sc in the structure of the Al_3Mg_2 phase further increases the binding energy with H (Supplementary Fig. 17c,d). Experimental evidences were further provided by thermal desorption spectroscopy (Supplementary Fig. 18) and time-of-flight secondary-ion mass spectrometry (TOF-SIMS) results (Supplementary Fig. 19) to support the high H-trapping capacity of Samson-$Al_3(Mg, Sc)_2$ nanophase. In combination, these explain the unprecedented H-trapping capacity achieved in the nanosized Samson-$Al_3(Mg, Sc)_2$ phase, responsible for the extraordinary HE resistance observed in Al–Mg–Sc-II (Fig. 3c,d). Although other microstructural features (including the vacancies, dislocations and grain boundaries) make a much less contribution to the H-trapping (Supplementary Fig. 20 and Supplementary Note 2).

Conclusion and outlook

Size-dependent phase transformation leads to a dual distribution of nanoprecipitates, in which fine Al_3Sc (size below 10 nm and a number density of about 2.4×10^{21} m^{-3}) makes main contribution to strengthening, whereas the large $Al_3(Mg, Sc)_2/Al_3Sc$ (size above 10 nm and a number density of about 5.6×10^{21} m^{-3}) is responsible for the HE resistance. Without fine-sized or large-sized Al_3Sc nanoprecipitates, the necessary dual distribution of nanoprecipitates cannot be achieved and hence fails to optimize the strength–HE resistance combination (Supplementary Fig. 21a–d). From a materials design perspective, the optimal size range for the nanoprecipitates appears to be around 20 ± 10 nm (Fig. 2a) to ensure a synergy of strengthening response derived from smaller nanoprecipitates, and HE resistance from a higher volume fraction of the $Al_3(Mg, Sc)_2$ phase. We found the Mg content within the range from 4.5 wt% to 7.5 wt% also shows a HE resistance close to the 6.0 wt% Al–Mg–Sc-II alloy (Supplementary Fig. 21e). There is an optimum also for the heat treatment time, because the precipitation reaction of interest is diffusion-mediated, and as seen in Fig. 2a, after only 36 h κ reaches a plateau at a lower value than after 72 h, leading to an inferior HE resistance (Supplementary Fig. 21f).

We have confirmed that the strategy proposed here can be deployed to a twin-roll cast Al–Mg–Ti–Zr-II alloy, in which Ti and Zr replace Sc (Supplementary Fig. 22), Al–Mg–Cu–Sc-II alloy, in which the Cu addition further increases the strength of the alloy, and Al–Mg–Zn–Sc-II alloy in which the addition of a low concentration of Zn improves the mechanical properties (Supplementary Fig. 23). We also demonstrate that our approach can be scaled up, as we have prepared the Al–Mg–Sc-II alloy by using water-cooled copper mould casting and optimized thermomechanical processing. The scale-up alloy showed HE resistance close to the Al–Mg–Sc-II alloy, along with an increase of about 10% in tensile strength (Fig. 3c,d and Supplementary Fig. 24). Beyond these more conventional compositions, we can optimistically expect that the present design strategy can be applied also to newly proposed crossover Al alloys[43], advanced Al alloys prepared by additive manufacturing[44,45] and will provide opportunities for the development of high-strength H-tolerant Al alloys that could be readily adopted to large-scale industrial production.

Online content

Any methods, additional references, Nature Portfolio reporting summaries, source data, extended data, supplementary information, acknowledgements, peer review information; details of author contributions and competing interests; and statements of data and code availability are available at https://doi.org/10.1038/s41586-025-08879-2.

1. Bond, G. M., Robertson, I. M. & Birnbaum, H. K. The influence of hydrogen on deformation and fracture processes in high-strength aluminum alloys. *Acta Metall.* **35**, 2289–2296 (1987).
2. Scully, J. R., Young, G. A. & Smith, S. W. in *Gaseous Hydrogen Embrittlement of Materials in Energy Technologies* (eds Gangloff, R. P. & Somerday, B. P.) 707–768 (Woodhead Publishing, 2012).
3. Liu, X. M. et al. Transmission electron microscopic observations of embrittlement of an aluminum alloy by liquid metal. *Mater. Sci. Eng. A* **55**, 851–857 (1999).
4. Zhao, H. et al. Hydrogen trapping and embrittlement in high-strength Al alloys. *Nature* **602**, 437–441 (2022).
5. Wang, Y. et al. Switching nanoprecipitates to resist hydrogen embrittlement in high-strength aluminum alloys. *Nat. Commun.* **13**, 6860 (2022).
6. Xu, Y. T. et al. Suppressed hydrogen embrittlement of high-strength Al alloys by Mn-rich intermetallic compound particles. *Acta Mater.* **236**, 118110 (2022).
7. Knipling, K. E., Dunand, D. C. & Seidman, D. N. Criteria for developing castable, creep-resistant aluminum-based alloys – a review. *Z. Metall.* **97**, 246–265 (2006).
8. Liu, G. et al. Experiment and multiscale modeling of the coupled influence of constituents and precipitates on the ductile fracture of heat-treatable aluminum alloys. *Acta Mater.* **53**, 3459–3468 (2005).
9. Urban, K. & Feuerbacher, M. Structurally complex alloy phases. *J. Non Cryst. Solids* **334**, 143–150 (2004).
10. Dubois, J. M. & Belin-Ferré, E. (eds) *Complex Metallic Alloys: Fundamentals and Applications* (Wiley, 2010).
11. Samson, S. The crystal structure of the phase β-Mg_2Al_3. *Acta Crystal.* **19**, 401–413 (1965).
12. Feuerbacher, M. et al. The Samson phase, β-Mg_2Al_3, revisited. *Z. Kristal.* **222**, 259–288 (2007).
13. Blatov, V. A., Llyushin, G. D. & Proserplo, D. M. Nanocluster model of intermetallic compounds with giant unit cells: β, β′-Mg_2Al_3 polymorphs. *Inorg. Chem.* **49**, 1811–1818 (2010).
14. Chen, Y.-S. et al. Observation of hydrogen trapping at dislocations, grain boundaries, and precipitates. *Science* **367**, 171–175 (2020).
15. Yan, J. & Hodge, A. M. Study of β precipitation and layer structure formation in Al 5083: the role of dispersoids and grain boundaries. *J. Alloys Compd.* **703**, 242–250 (2017).
16. Deschamps, A. & Hutchinson, C. R. Precipitation kinetics in metallic alloys: experiments and modeling. *Acta Mater.* **220**, 117338 (2021).
17. Norman, A. F., Prangnell, P. B. & McEwen, R. S. The solidification behaviour of dilute aluminium–scandium alloys. *Acta Mater.* **46**, 5715–5732 (1998).
18. Tan, L. & Allen, T. R. Effect of thermomechanical treatment on the corrosion of AA5083. *Corros. Sci.* **52**, 548–554 (2010).
19. D'Antuono, D. S. et al. Grain boundary misorientation dependence of β phase precipitation in an Al-Mg alloy. *Scripta Mater.* **76**, 81–84 (2014).
20. Liu, G. et al. Nanostructured high-strength molybdenum alloys with unprecedented tensile ductility. *Nat. Mater.* **12**, 344–350 (2013).
21. Herbig, M. et al. Atomic-scale quantification of grain boundary segregation in nanocrystalline material. *Phys. Rev. Lett.* **112**, 126103 (2014).
22. Marquis, E. A., Seidman, D. N., Asta, M. & Woodward, C. Composition evolution of nanoscale Al_3Sc precipitates in an Al–Mg–Sc alloy: experiments and computations. *Acta Mater.* **54**, 119–130 (2006).
23. Hutchinson, C. R., Fan, X., Pennycook, S. J. & Shiflet, G. J. On the origin of the high coarsening resistance of Ω plates in Al–Cu–Mg–Ag Alloys. *Acta Mater.* **49**, 2827–2841 (2001).
24. Reich, L., Murayama, M. & Hono, K. Evolution of Ω phase in an Al–Cu–Mg–Ag alloy—a three-dimensional atom probe study. *Acta Mater.* **46**, 6053–6062 (1998).
25. Xue, H. et al. Highly stable coherent nanoprecipitates via diffusion-dominated solute uptake and interstitial ordering. *Nat. Mater.* **22**, 434–441 (2023).
26. Fu, L. et al. Mechanical properties of $L1_2$ type Al_3X (X=Mg, Sc, Zr) from first-principles study. *Phys. Stat. Sol. b* **249**, 1510–1516 (2012).
27. Foley, D. L., Leff, A. C., Lang, A. C. & Taheri, M. L. Evolution of β-phase precipitates in an aluminum-magnesium alloy at the nanoscale. *Acta Mater.* **185**, 279–286 (2020).
28. Orthacker, A. et al. Diffusion-defining atomic-scale spinodal decomposition within nanoprecipitates. *Nat. Mater.* **17**, 1101–1107 (2018).
29. Clouet, E. et al. Complex precipitation pathways in multicomponent alloys. *Nat. Mater.* **5**, 482–488 (2006).
30. Røyset, J. & Ryum, N. Scandium in aluminium alloys. *Inter. Mater. Rev.* **50**, 19–44 (2005).
31. Aboulfadl, H. et al. Dynamic strain aging studied at the atomic scale. *Acta Mater.* **86**, 34–42 (2015).
32. da Silva, A. K. et al. Phase nucleation through confined spinodal fluctuations at crystal defects evidenced in Fe-Mn alloys. *Nat. Commun.* **9**, 1137 (2018).
33. Legros, M., Dehm, G., Arzt, E. & Balk, T. J. Observation of giant diffusivity along dislocation cores. *Science* **319**, 1646–1649 (2008).
34. Han, Y. et al. Influence of hydrogen content on the microstructure and mechanical properties of ER5183 wires. *Adv. Mater. Sci. Eng.* **2019**, 362369 (2019).
35. Safyari, M., Moshtaghi, M., Kuramoto, S. & Hojo, T. Influence of microstructure-driven hydrogen distribution on environmental hydrogen embrittlement of an Al-Cu-Mg alloy. *Inter. J. Hydro. Energy* **46**, 37502–37508 (2021).
36. Tadakazu, O. et al. Effects of hydrogen on tensile properties of Al-8%Mg alloy. *J. Jpn Inst. Light Met.* **27**, 473–479 (1977).
37. Breen, A. J. et al. Solute hydrogen and deuterium observed at the near atomic scale in high-strength steel. *Acta Mater.* **188**, 108–120 (2020).
38. Chang, Y. H. et al. Characterizing solute hydrogen and hydrides in pure and alloyed titanium at the atomic scale. *Acta Mater.* **150**, 273–280 (2018).
39. Gault, B. et al. Towards establishing best practice in the analysis of hydrogen and deuterium by atom probe tomography. *Microsc. Microanal.* **30**, 1205–1220 (2024).
40. Safyari, M., Moshtaghi, M., Hojo, T. & Akiyama, E. et al. Mechanisms of hydrogen embrittlement in high-strength aluminum alloys containing coherent or incoherent dispersoids. *Corros. Sci.* **194**, 109895 (2022).
41. Safyari, M. et al. New insights into hydrogen trapping and embrittlement in high strength aluminum alloys. *Corros. Sci.* **223**, 111453 (2023).

42. Takahashi, J., Kawakami, K. & Kobayashi, Y. Origin of hydrogen trapping site in vanadium carbide precipitation strengthening steel. *Acta Mater.* **153**, 193–204 (2018).
43. Stemper, L. et al. On the potential of aluminum crossover alloys. *Prog. Mater Sci.* **124**, 100873 (2022).
44. Kürnsteiner, P. et al. Control of thermally stable core-shell nano-precipitates in additively manufactured Al-Sc-Zr alloys. *Addit. Manuf.* **32**, 100910 (2020).
45. Jia, Q. B. et al. Selective laser melting of a high strength Al–Mn–Sc alloy: alloy design and strengthening mechanisms. *Acta Mater.* **171**, 108–118 (2019).
46. Safyari, M. et al. Manipulating nanostructure during wire arc additive manufacturing defeats hydrogen embrittlement. *Corr. Sci.* **233**, 112088 (2024).

Methods

Materials fabrication

Alloys with nominal composition of Al–6.0 wt% Mg (Al–Mg), Al-6.0 wt% Mg–0.3 wt% Sc (Al–Mg–Sc) and Al–0.3 wt% Sc (Al–Sc) were, respectively, melted by using 99.99 wt% pure Al, 99.99 wt% pure Mg and master Al–2.0 wt% Sc alloy. The Zr content in the Al–Sc master alloy is only 66 ppmw. An Al–Ti–B grain refiner was added to the melt, followed by degassing and removal of the slag. Twin-roll casting with water-cooled Cu-Be rollers was used to prepare the Al–Mg, Al–Mg–Sc and Al–Sc alloy strips, in which the initial rolling speed, melt temperature, nozzle width and cooling water pressure were 3.0 m min^{-1}, 690 °C, 200 mm and 0.4 MPa, respectively, leading to 5 mm-thick alloy strips. Specimens were cut from the strips and subsequently exposed to first-step heat treatment at 400 °C for 4 h, followed by water quenching. Some specimens were further annealed at 250 °C for 72 h or 36 h, which is the second-step heat treatment. The maximum error of all temperatures in the present experiments was ±2 °C. For comparison, four commercial 5xxx series alloys were used to study their resistance to HE. The four alloys are 5052, 5083, 5754 and 5A06, all provided by the Aluminium Corporation of China (CHINALCO). The chemical composition and treatment condition are given in Extended Data Table 1.

Microstructural characterization

To study the microstructures at the nanoscale, high-angle annular dark field (HAADF) scanning transmission electron microscopy (STEM) and energy-dispersive X-ray analysis (Bruke Super-X, Bruke) were performed using Cs-STEM (FEI cubed Themis, Thermo Fisher Scientific) operating at 300 kV. TEM foils were prepared by following standard electropolishing techniques for Al alloys[8,25]. Samples for TEM observations were sliced into 0.3-mm-thick pieces using a slow-speed saw, punched into 3 mm diameter discs and ground to about 60 μm thickness. Electropolishing was conducted using Struers Tenupol-5 twin-jet electropolishing machine with a 5% perchloric acid in ethanol at −30 °C and 15 V. Parameters of the spherical-like nanoprecipitates, including size, number density and volume fraction, were statistically measured within the TEM micrographs with the electron beam oriented parallel to the $[100]_{Al}$ zone axis. The number density, N_V, is determined using[47]

$$N_V = \frac{N}{(t+d)}, \quad (1)$$

where N is the number of counted nanoprecipitates on the TEM images, t is the thickness of the foil area and d is the measured mean diameter. The foil thickness was determined using electron energy loss spectroscopy thickness mapping[48], which was conducted in the TEM mode. The volume fraction is estimated as

$$f = \frac{4N_V\pi d^3}{3}. \quad (2)$$

A scanning electron microscope (SEM, FEI-Verios 460) with electron backscattered diffraction was used to analyse the grain structure. The specimens for the electron backscattered diffraction observations were prepared by electropolishing using an electrolyte consisting of 10 vol% perchloric acid ($HClO_4$) and 90 vol% absolute ethanol (C_2H_5OH) at −30 °C for 1 min at an operation voltage of 25 V.

APT experiments were performed using a Local Electrode Atom Probe (LEAP 4000HR) from CAMECA. Specimens for APT were prepared by wire-cutting small blanks (0.3 × 0.3 × 10 mm^3) using a combination of slicing and mechanical grinding. A two-step electropolishing procedure was subsequently used for the preparation of APT tips, a 10 vol% perchloric acid in methanol solution was used for rough polishing, and the final polishing was performed using a solution of 2 vol% perchloric acid in butoxyethanol. APT data collection was done at a specimen temperature of 30 ± 0.3 K, and tomographic reconstruction and analysis of APT data were carried out using IVAS 6 software. APT examinations were performed in different modes. In the high-voltage mode, the voltage pulse fraction (pulse voltage/steady-state direct current voltage) was 19%, the pulse frequency was 200 kHz and the background gauge pressure was less than 6.7×10^{-8} Pa (5×10^{-10} torr). Laser mode was also adopted, at a set-point temperature of 30 K and under ultrahigh vacuum at a pressure below 2.0×10^{-9} Pa (1.5×10^{-11} torr). The laser kept a pulse repetition rate of 250 kHz, and the energy was calibrated for each individual tip to yield an equivalent pulse fraction in voltage mode of 20%, which corresponded to laser energy between 75 pJ and 160 pJ. The detection rate was set to have 0.5% of the applied laser pulses resulting in an evaporation event. In cryo-APT experiments, specimens were prepared by cryo-plasma focused-ion beam (PFIB) on an FEI Helios PFIB instrument operated with an Xe source to avoid contamination by gallium. The cryo-prepared APT specimens were transferred from the PFIB into APT under cryogenic ultrahigh vacuum conditions using cryogenic ultrahigh vacuum sample transfer protocols[4]. In APT data analysis, the concentration of each element, I, in at% is estimated from the number of atoms of each element, n_i, divided by the total number of atoms in the sample volume (n_T), that is, $c_i = n_i/n_T$. The standard error of this estimate is given[49] by $\sigma = \sqrt{c_i \times (1 - c_i)/n_i}$.

Electrochemical experiments

The samples were polished with SiC emery paper to a 2000 grit finish, followed by cleaning the corroded surfaces with ethanol and drying them for additional analysis. Potentiodynamic polarization curves and electrochemical impedance spectroscopy (EIS) were measured by the CS300M potentiostat (Corrtest Instrument). All the electrochemical measurements were carried out in 3.5 wt% NaCl solution at room temperature. A standard three-electrode cell was used, in which the specimens under investigation, each with an exposed area of 1 cm^2, were designated as the working electrode, a platinum (Pt) wire was used as the counterelectrode and a saturated calomel electrode (SCE) was used as the reference electrode. Every electrochemical measurement was carried out at least three times to ensure the repeatability of the findings. Potentiodynamic polarization was preceded by a 30-min open circuit potential (OCP) test when the OCP value of the sample in NaCl solution tends to approach a condition of relative balance. The EIS tests were conducted using an amplitude of 10 mV RMS (root mean square) sinusoidal perturbation with respect to OCP, and the frequency range was 105 Hz to 10^{-2} Hz. Since then, at a scan rate of 0.5 mV s^{-1}, the charged potential changes from OCP to −200 mV and 200 mV (compared with SCE), respectively. CorrTest-CSAnalysis, a commercial program, was used to match the experimental impedance spectra.

Synchrotron X-ray diffraction measurements

High-energy X-ray diffraction experiments were conducted at the beamline BL12SW of Shanghai Synchrotron Radiation Facility, China. The X-ray wavelength was 0.1242 Å with an energy of 97.76 keV, and a beam size of 1 mm × 1 mm. The standard sample LaB6 was tested to evaluate the instrumental broadening.

Positron annihilation lifetime spectroscopy experiments

Positron annihilation lifetime spectroscopy experiments were performed at the Institute of High Energy Physics of the Chinese Academy of Sciences to measure the vacancy concentration[50] in the Al–Mg–Sc-II alloy. The spectra comprise at least 2 million counts, and the time resolution of the system is about 208 ps. A program MELT 4.0 was used to analyse the positron lifetime[50]. The energies of annihilating γ-ray pairs (denoted by E_1 and E_2) were simultaneously recorded by the two detectors located at an angle of 180° relative to each other. The difference in energies of the two γ-rays $\Delta E = E_1 - E_2$ is expressed as cP_L and the total energy $E_t = E_1 + E_2$ is expressed as $2m_0c^2 - E_B$ (neglecting the thermal energies and chemical potentials), where P_L is the longitudinal component of the positron-electron momentum along the direction of the γ-ray emission, c is the speed of light, m_0 is the electron rest mass and E_B is

the electron binding energy. A total count of more than 2×10^7 for each measurement was accumulated for 12 h.

H-charging and tensile test

The susceptibility to H embrittlement of the present Al alloys was evaluated by H precharging and slow strain rate tensile tests conducted at room temperature at an initial strain rate of 1×10^{-5} s^{-1}. Tensile specimens with a gauge length of 15 mm and a thickness of 1.4 mm were used. At least three samples were tested for each condition (uncharged and H-charged). Before the slow strain rate tensile test, electrochemical H charging was performed on tensile specimens in an aqueous solution containing 0.3 wt% NaCl and 0.3 wt% CH_4N_2S at room temperature. The platinum foil served as the anode and the surface of the gauge length of the specimens served as the cathode during H charging. The H-charging experiment was performed at a current density of 5 mA cm^{-2} and a charging time of 48 h for each tensile specimen. The time interval between the end of H precharging and the start of tensile testing was less than 6 min to avoid H loss.

The hydrogen concentration in present Al alloys (uncharged and H-charged) were measured by thermal desorption spectroscopy (TDS); the size of the TDS specimens is the same as the gauge length segment of the previous tensile specimens ($15 \times 3.5 \times 1.4$ mm^3), which were subjected to the same H-precharging condition as that for tensile specimens. During the TDS test, the specimen was heated from room temperature to 550 °C at a heating rate of 90 °C h^{-1}, and the total H concentration was determined by measuring the cumulative desorbed H from room temperature to 500 °C. Three samples were measured for each condition in the H-charged and uncharged states. When using the TDS to experimentally measure the H-binding energy, different heating rates were used, and the Choo–Lee method[51] was adopted to quantitatively determine the E_d.

TOF-SIMS examinations

The TOF-SIMS elemental mapping was performed with an AMBER GMU TOF-SIMS (manufactured by Tescan) instrument, which is equipped with a standard FIB-SEM system. Before the TOF-SIMS analysis, the contaminated layer on the sample was removed by pre-bombarding the sample surface with FIB. The final test parameters were chosen as follows: 30 kV accelerating voltage and beam intensity of 50 pA. Characteristic mass peaks of the ground paint are those of Mg and Sc in positive ion mode and H in negative ion mode.

First-principles theory calculations

First-principles theory calculations were conducted within the DFT framework using the Vienna ab initio simulation package[52,53], in which the ion–electron interactions were described by the projector augmented wave method[54] and the GGA-PBE exchange correlation functionals[55] were used. The integration in the Brillouin zone was performed on a Γ-centred k-mesh with a grid density of 8,000. A cutoff in plane-wave energy of 520 eV was applied using a first-order Methfessel–Paxton scheme[56] with a smearing parameter of 0.2 eV. The total energy was converged within 10^{-6} eV per atom for all calculations. And the relaxed configurations were obtained using the conjugate gradient method, which terminated the search when the force on all atoms was reduced to 0.01 eV $Å^{-1}$. Atomic configurations were visualized using Diamond[57].

A 1168-atom cubic supercell with the lattice constant $a = 2.8239$ nm, containing many partially occupied and split atomic positions, was adopted to model the β-Al_3Mg_2 phase, whereas an 879-atom rhombohedral supercell with $a = 1.9968$ nm and $c = 4.8911$ nm was for the β′-Al_3Mg_2 phase (Extended Data Table 2), according to the literature[12,58–60]. The chemical (substitutional) disorder was obtained by following the recipes of Monte Carlo special quasi-random structure (MCSQS)[61] within the ATAT codes[62].

The basic calculation method for the trapping energy of H (E_b) is the same as in refs. 63,64. Considering the quite large number of calculations, we only calculated totally 28 typical configurations doping 1 H atom for each phase, in which the nearest neighbour for the site of H containing five types: 4 Mg atoms, 1 Al and 3 Mg, 2 Al and 2 Mg, 3 Al and 1 Mg, and 4 Al atoms, respectively.

For both two phases, the deep hydrogen trap sites were found with the NN of 4 Mg atoms, for example, the values of E_b are 1.12 eV for the β-Al_3Mg_2 phase and 0.85 eV for the β′-Al_3Mg_2 phase, which indicates that the β-Al_3Mg_2 phase thermodynamically shows a larger tendency to trap H atom than the β′-Al_3Mg_2 phase.

Data availability

All data supporting the findings of this study are available in the paper and Supplementary Information. Additional images are available from the corresponding author upon request.

47. Yang, C. et al. The influence of Sc solute partitioning on the microalloying effect and mechanical properties of Al-Cu alloys with minor Sc addition. *Acta Mater.* **119**, 68–79 (2016).
48. Malis, T., Cheng, S. C. & Egerton, R. F. EELS log-ratio technique for specimen-thickness measurement in the TEM. *J. Electron Micros. Tech.* **8**, 193–200 (1988).
49. Miller, M. K. & Forbes, R. G. *Atom–Probe Tomography: The Local Electrode Atom Probe* (Springer, 2014).
50. Wu, S. H. et al. Freezing solute atoms in nanograined aluminum alloys via high-density vacancies. *Nat. Commun.* **13**, 3495 (2022).
51. Choo, W. Y. & Lee, J. Y. Thermal analysis of trapped hydrogen in pure iron. *Metall. Trans. A* **13**, 135–140 (1982).
52. Kresse, G. & Furthmüller, J. Efficient iterative schemes for ab initio total-energy calculations using a plane-wave basis set. *Phys. Rev. B Condens. Matter* **54**, 11169–11186 (1996).
53. Kresse, G. & Furthmüller, J. Efficiency of ab-initio total energy calculations for metals and semiconductors using a plane-wave basis set. *Comput. Mater. Sci.* **6**, 15–50 (1996).
54. Kresse, G. & Joubert, D. From ultrasoft pseudopotentials to the projector augmented-wave method. *Phys. Rev. B* **59**, 1758–1775 (1999).
55. Perdew, J. P., Burke, K. & Ernzerhof, M. Generalized gradient approximation made simple. *Phys. Rev. Lett.* **77**, 3865–3868 (1996).
56. Methfessel, M. & Paxton, A. T. High-precision sampling for Brillouin-zone integration in metals. *Phys. Rev. B* **40**, 3616–3621 (1989).
57. Pennington, W. T. DIAMOND–visual crystal structure information system. *J. Appl. Crystallogr.* **32**, 1028–1029 (1999).
58. Mizutani, U. et al. Fermi surface-Brillouin-zone-induced pseudogap in γ-$Mg_{17}Al_{12}$ and a possible stabilization mechanism of β-Al_3Mg_2. *J. Phys. Condens. Matter* **22**, 485501 (2010).
59. Wolny, J. & Duda, M. Ordering of hexagonal layers in phase β- and β′-Mg_2Al_3. *Philos. Mag.* **91**, 1568–1580 (2011).
60. Vrtnik, S. et al. Stabilization mechanism of γ-$Mg_{17}Al_{12}$ and β-Mg2Al3 complex metallic alloys. *J. Phys. Condens. Matter* **25**, 425703 (2013).
61. van de Walle, A. et al. Efficient stochastic generation of special quasirandom structures. *Calphad* **42**, 13–18 (2013).
62. van de Walle, A., Asta, M. & Ceder, G. The alloy theoretic automated toolkit: a user guide. *Calphad* **26**, 539–553 (2002).
63. Tsuru, T. et al. First-principles study of hydrogen segregation at the $MgZn_2$ precipitate in Al-Mg-Zn alloys. *Comput. Mater. Sci.* **148**, 301–306 (2018).
64. Yamaguchi, M. et al. Hydrogen trapping in Mg_2Si and Al_7FeCu_2 intermetallic compounds in aluminum alloy: first-principles calculations. *Mater. Trans.* **61**, 1907–1911 (2020).

Acknowledgements This work was supported by the National Natural Science Foundation of China (grant nos. U23A6013, 92360301, U2330203 and 52071260), the National Key Research and Development Program of China (2024YFB3714000), the Open Research Fund of Shannxi Laboratory of Advanced Materials, and the 111 Project of China (BP2018008). This work is also supported by the International Joint Laboratory for Micro/Nano Manufacturing and Measurement Technologies. We acknowledge S. C. Cao and K. Yang for assistance in performing high-energy X-ray diffraction experiments at Shanghai Synchrotron Radiation Facility (BL13W1 and BL12SW beamline), and C. Yang, P. Zhang, H. Xue and S. H. Wu (Xi'an Jiaotong University) for their assistance in experiments.

Author contributions Y.X., G.L., B.G. and J.S. initiated and supervised the project. S. Jiang and R.W. prepared the materials and carried out the microstructural/structural analysis. Y.X., H.T. and X.J. performed H-charging experiments and the mechanical property testing. S. Jiang, R.W., S. Jin, X.C. and B.G. conducted the APT examinations. C.G. and Y.P. assisted with the HAADF examinations. F.L. and M.W. carried out the DFT calculations. G.T. performed the TDS experiments. X.L., S.Z. and H.W. assisted with the material preparation. All authors discussed the data. G.L., Y.X., B.G. and J.S. wrote the paper.

Competing interests The authors declare no competing interests.

Additional information

Supplementary information The online version contains supplementary material available at https://doi.org/10.1038/s41586-025-08879-2.

Correspondence and requests for materials should be addressed to Yuantao Xu, Gang Liu, Baptiste Gault or Jun Sun.

Peer review information *Nature* thanks Lijie Qiao and the other, anonymous, reviewers for their contribution to the peer review of this work.

Extended Data Table 1 | Chemical composition of the commercial 5xxx alloys used in this work

Alloys	Mg	Cu	Mn	Si	Ti	Cr	Fe	Al	Condition (thickness)
5052	2.64	0.07	0.07	0.21	–	0.22	0.23	Balance	Cold-rolled sheet in 5.0 mm
5754	3.15	0.11	0.52	0.41	0.15	0.35	0.06	Balance	Cold-rolled sheet in 5.0 mm
5083	4.53	0.07	0.73	0.31	0.07	0.12	0.41	Balance	Cold-rolled sheet in 6.0 mm
5A06	6.23	0.08	0.62	0.23	0.03	–	0.05	Balance	Cold-rolled sheet in 6.0 mm

Extended Data Table 2 | Crystal structure parameters used to calculate trapping energy

Phase	Space group	Space group number	Lattice constant	Supercell	K-point sampling
β- Al_3Mg_2	$Fd\bar{3}m$	(227)	a = 2.8239 nm	1×1×1	1×1×1
β'- Al_3Mg_2	R3m	(160)	a = 1.9968 nm c = 4.8911 nm	1×1×1	2×2×1